Published in final edited form as:
J Am Chem Soc. 2011 May 18; 133(19): 7256–7259. doi:10.1021/ja111742z.

Characterization of a High-Spin Nonheme Fe^{III}–OOH Intermediate and Its Quantitative Conversion to an Fe^{IV}=O Complex

Feifei Li[1], **Katlyn K. Meier**[2], **Matthew A. Cranswick**[1], **Mrinmoy Chakrabarti**[2], **Katherine M. Van Heuvelen**[1], **Eckard Münck**[2,*], and **Lawrence Que Jr.**[1,*]

[1] Department of Chemistry and Center for Metals in Biocatalysis, University of Minnesota, Minneapolis, MN 55455

[2] Department of Chemistry, Carnegie Mellon University, Pittsburgh, PA 15213

Abstract

We have generated a high-spin Fe^{III}–OOH complex supported by tetramethylcyclam via protonation of its conjugate base and characterized it in detail by various spectroscopic methods. This Fe^{III}–OOH species converts quantitatively to an Fe^{IV}=O complex via O–O bond cleavage, which represents the first example of such a conversion. This conversion is promoted by two factors: the strong Fe^{III}–OOH bond that inhibits Fe–O bond lysis and the addition of protons that facilitate O–O bond cleavage. This example provides a synthetic precedent for how O–O bond cleavage of high-spin iron(III)-peroxo intermediates of nonheme iron enzymes may be promoted.

Cleavage of the O–O bond of iron(III)-hydroperoxo (Fe^{III}–OOH) species is a key step in the O_2 activation mechanisms of cytochrome P450,[1] Rieske dioxygenases,[2] and even methane monooxygenase (MMO),[3] leading to high-valent iron-oxo species that effect organic substrate oxidation. On the other hand, Fe–O bond cleavage must occur to release H_2O_2 in the catalytic cycle of superoxide reductase (SOR)[4] and for cytochrome P450 reactions that exhibit uncoupling.[1] While protonation of the proximal O atom of the Fe^{III}–OOH unit can be readily envisioned as the step needed to release H_2O_2, the mechanism for O–O bond cleavage is not as simple. For heme peroxidases and cytochrome P450, it is generally accepted that protonation of the distal O atom of the low-spin Fe^{III}–OOH intermediate facilitates the heterolysis of the O–O bond.[1] This notion should also apply to nonheme iron systems, but the likely *high-spin* state of iron-peroxo species in nonheme enzymes could raise the barrier for O–O bond lysis relative to that for *low-spin* counterparts in heme enzymes.[5] The scarcity of experimental evidence further limits insights into O–O bond scission by nonheme enzymes. The only mechanistically relevant information available is for MMO, where the conversion of the peroxodiiron(III) intermediate to the diiron(IV) oxidant exhibits a pH dependence and a H/D solvent kinetic isotope effect,[3] emphasizing the key role played by a proton in O–O bond cleavage. Among synthetic complexes, there are only a few nonheme Fe^{III}–OOH complexes that are spectroscopically well characterized,[6,7] but none of them has been directly observed to generate a high-valent iron-oxo intermediate, thus making it difficult to obtain mechanistic insights into this key step in iron-catalyzed oxygen activation.

emunck@cmu.edu, larryque@umn.edu.

Supporting Information Available: Detailed experimental procedures and physical methods, a plot for the interconversion between **1** and **2**, a more extensive discussion of the Mössbauer and EPR simulations of **1** and **2**, details of the EXAFS analysis, and an Eyring plot for conversion of **2** to **3**. This material is available free of charge via the internet at http://pubs.acs.org.

To obtain the first example of a Fe^{III}–OOH complex that can undergo O–O bond cleavage to generate a high-valent iron-oxo complex, we have focused on trapping $[Fe^{III}(TMC)(OOH)]^{2+}$ (**2**; see Scheme 1A for a structure of TMC), a yet elusive species invoked in the reactions of O_2 with $[Fe^{II}(TMC)(CH_3CN)]^{2+}$ that afford $[Fe^{IV}(O)(TMC)(CH_3CN)]^{2+}$ (**3**) in 60–80% yield as the final product.[8] Herein we report the high-yield generation of **2** by protonation of the previously reported $[Fe^{III}(TMC)(O_2)]^{+}$ complex (**1**)[9] at −40 °C, its detailed spectroscopic characterization, and kinetic studies that shed mechanistic light on the quantitative conversion of **2** to **3** (Scheme 1B).

Complex **1** was generated using the published procedure[7] by treating 2.0 mM $[Fe^{II}(TMC)(CH_3CN)]^{2+}$ in CH_3CN with 10 equiv. NEt_3 followed by 20 equiv. H_2O_2 in CH_3CN at −40 °C. Complex **1** exhibits a λ_{max} of 835 nm (Figure 1 left panel) with an ε value of 650 $M^{-1}cm^{-1}$, established with the aid of Mössbauer data (*vide infra).* Upon addition of 20 equiv. $HClO_4$ at −40 °C, **1** converted immediately to a short-lived ($t_{1/2}$ ~ 1 min) maroon intermediate (**2**) with a shoulder-like absorption feature at ~500 nm (ε = 450 $M^{-1}cm^{-1}$), which in turn decayed to give the signature absorption feature of **3** (Figure 1). The significant blue shift observed in the conversion of **1** to **2** has been noted previously in the protonation of other nonheme $Fe^{III}(\eta^2\text{-}O_2)$ species, consistent with the weaker basicity of the hydroperoxo monoanion compared to the peroxo dianion.[6a–b] The conversion of **1** to **2** is reversible. Addition of excess NEt_3 to the solution of **2** instantly results in the near-quantitative regeneration of **1**, as shown by its characteristic absorption band. This cycle can be repeated several times (see Figure S1). These results further underscore that **2** is the conjugate acid of **1** and can be formulated as $[Fe^{III}(TMC)(OOH)]^{2+}$.

The Mössbauer samples of **1**, **2** and **3** contain large fractions of the designated complexes. In the spectrum of **1** shown in Figure 2A, about 90% of total Fe belongs to **1**, while 80% of the Fe in Figure 2B can be assigned to **2** with 10% of the iron belonging to Fe^{IV}=O complex **3** (*vide infra* for analysis details). Analysis of a sample of **2** that was allowed to decay for 5 min after addition of $HClO_4$ shows that 90% of the total Fe corresponds to **3** (Fig. S9). Thus, *the overall conversion of **1** to **3** is essentially quantitative*.

The electronic structures of **1** and **2** were established by EPR and Mössbauer spectroscopy. Both complexes are high-spin Fe^{III} with quite different zero field splitting (ZFS) parameters and isomer shifts (Table S1). We have analyzed the data with the S = 5/2 spin Hamiltonian, eq 1,

$$\mathcal{H}=D(S_z^2-35/4)+E(S_x^2-S_y^2)+\beta\boldsymbol{S}\cdot\boldsymbol{g}\cdot\boldsymbol{B}+\boldsymbol{S}\cdot\boldsymbol{A}\cdot\boldsymbol{I}-g_n\beta_n\boldsymbol{B}\cdot\boldsymbol{I}+\mathcal{H}_Q$$

where D and E are the axial and rhombic ZFS parameters, A is the ^{57}Fe magnetic hyperfine tensor and $\mathcal{H}_Q$ describes the nuclear quadrupole interactions.

The X-band EPR spectrum of **1** exhibits, for the middle Kramers doublet, signals at g_{eff} = 4.58, 4.38, and ≈ 4.1 (Figures 3A and S4–7). Mössbauer analysis (details in Supporting Information) shows that $D \approx -0.9$ cm^{-1} and E/D = 0.28(1). With E/D fixed, the explanation of the EPR features of **1** requires inclusion of substantial fourth-order ZFS parameters, eq 2.

$$H_{4th}=\frac{F}{180}[35S_z^4-30S(S+1)S_z^2+25S_z^2-6S(S+1)-3S^2(S+1)^2]+\frac{a}{6}[S_x^4+S_y^4+S_z^4-\frac{1}{5}S(S+1)(3S^2+3S-1)]$$

For the simulation of Figure 3A, we used $F = -0.108$ cm^{-1} and $a = -0.017$ cm^{-1}. Large fourth-order parameters, namely $a = 0.074$ cm^{-1} and $F = 0.043$ cm^{-1}, have been reported for Fe superoxide dismutase-azide,[10] together with $D = 0.46$ cm^{-1} and $E/D = 0.255$. An 8.0 T Mössbauer spectrum of **1** together with a spectral simulation is shown in Figure 2A (see Figures S2 and S3 for additional spectra). The shoulder on the low energy feature (at ~ −6 mm/s Doppler velocity) and the fairly sharp high-energy line show that the ^{57}Fe A-tensor is anisotropic. The spectrum shown gives a value for the isomer shift of **1**, $\delta = 0.58$ mm/s, similar to that of the side-on peroxo complex $[Fe^{III}(N4Py)(\eta^2\text{-}O_2)]^+$ ($\delta = 0.61$ mm/s).[6b] See SI for additional details of the spectral analysis.

Analysis of the Mössbauer spectra of **2** shown in Figures 2B and S8 yielded $D = +2.5$ cm^{-1}, $E/D = 0.097(7)$ and $\delta = 0.51$ mm/s. The EPR spectrum of **2** exhibits signals at $g_{eff} = 8.00$ (ground doublet), 5.71 (middle) and 3.4 (ground), consistent with the above D and E/D values (Figure 3B). The parameters used for the simulations of **1** and **2** are listed in Table S1.

We also carried out Fe K-edge X-ray absorption spectroscopic (XAS) studies to obtain structural information and metric parameters for **1** and **2** (Figure 4, Tables S1–S3). The EXAFS spectrum of **1** is best fit by two N/O scatterers at 1.93 Å and four N/O scatterers at 2.20 Å, while the best fit for **2** consists of one N/O scatterer at 1.92 Å and four N/O scatterers at 2.15 Å. Interchanging the number of scatterers in the 1.9-Å sub-shells of **1** and **2**, which arise from the peroxo ligands, significantly worsened the overall fit quality for both complexes with unacceptable Debye-Waller factors for this sub-shell in both cases (Tables S2 and S3). These results lead to the respective assignments of an η^2-binding mode to the dianionic peroxo ligand in **1** and an η^1-binding mode to the monoanionic hydroperoxo ligand of **2**. This conclusion is supported by the observed 0.05-Å decrease in r(Fe-N_{TMC}) from **1** to **2**.[11]

Resonance Raman studies of **1** and **2** provide additional insight into how the difference in binding mode affects the two high-spin iron(III)-peroxo units. Resonance enhanced vibrations are found for **1** at 826 and 493 cm^{-1} and for **2** at 870 and 676 cm^{-1} (Figures 5 and S10). These features can be assigned respectively to ν(O–O) and ν(Fe–O) modes on the basis of downshifts observed upon ^{18}O-labeling, which conform to predictions for diatomic harmonic oscillators by Hooke's Law. The observed vibrational modes compare favorably to those reported for related complexes (Tables 1 and S4). The sole exception is the ν(Fe–O) of **2** at 676 cm^{-1}, which lies above the range of ν(Fe–O) values (420–620 cm^{-1}) found for other high-spin Fe^{III}–OOH complexes studied thus far (Table 1). We speculate that the high ν(Fe–O) value for **2** may reflect the weaker electron donating ability of the presumed CH_3CN ligand *trans* to the hydroperoxo unit relative to those of the other complexes in Table 1. The stronger Fe–O bond suggested by the high ν(Fe–O) value for **2** is also likely to be an important factor that contributes to the observed cleavage of its O–O bond. In contrast, the Fe^{III}–OOH units of oxyhemerythrin[12] and superoxide reductase (SOR),[13] with ν(Fe–O) values that are at least 100 cm^{-1} smaller, undergo Fe–O bond cleavage in the course of their respective functions.

After its formation from **1**, **2** quickly decayed and underwent O–O bond cleavage to form $[Fe^{IV}(O)(TMC)(CH_3CN)]^{2+}$ (**3**)[14] in essentially quantitative yield (*vide supra*). The decay of **2** (monitored at 500 nm) occurred concomitantly with the appearance of **3** (monitored at 820 nm), with an isosbestic point at ~695 nm (Figure 1 right panel). The time courses of the absorbance changes at both 500 and 820 nm could be fit with a simple first-order kinetic model (Figure 6 left panel), affording rate constants (k_{obs}) that were found to be identical within experimental error. The temperature dependence of the k_{obs} values was determined between −40 °C to −20 °C (Figure S11) and gave rise to an Eyring plot with activation

parameters of $\Delta H^{\ddagger}$ = 44(2) kJ/mol and $\Delta S^{\ddagger}$ = −90(10) J/mol·T. These parameters are quite distinct from those determined for the reaction of $[Fe^{II}(TMC)(CH_3CN)]^{2+}$ with H_2O_2 in CH_3CN in the presence of 2,6-lutidine to form **3** ($\Delta H^{\ddagger}$ = 29(2) kJ/mol and $\Delta S^{\ddagger}$ = −144(10) J/mol·T), which involves a direct Fe^{II}/Fe^{IV}=O conversion.[15] On the other hand, the intermediacy of the Fe^{III}–OOH complex **2** has been postulated in the reactions of $[Fe^{II}(TMC)(NCCH_3)]^{2+}$ with O_2 in the presence of an H-atom donor or its equivalent that afford **3** as the final product, but **2** has been elusive in these reactions.[8] Our results thus provide the first direct evidence to support this hypothesis.

This first unequivocal example of converting a high-spin Fe^{III}–OOH species to an Fe^{IV}=O complex provides an opportunity to discern what factors promote O–O bond cleavage in such species. Importantly, the conversion of **2** to **3** is found to be *proton-dependent*. [16] As shown in Figure 6 right panel, the values for both k_{obs}(500) and k_{obs}(820) increase linearly with [$HClO_4$] added, and a second-order rate constant k_2 of 0.9(1) $M^{-1}s^{-1}$ at −40 °C can be extracted from the slope of this plot. Also of significance is the observation that the quantitative yield of **3** from **1** is not affected even at the highest amounts of acid added, indicating that the added protons do not lead to Fe–O bond cleavage in **2** to release H_2O_2. The observed proton dependence in the formation of **3** strongly suggests that a proton promotes O–O bond cleavage.

Proton-assisted O–O bond cleavage has generally been associated with O–O bond heterolysis,[1,17,18] as protonation of the terminal oxygen atom of the Fe–OOH moiety converts hydroxide into a much better leaving group. Indeed this is the generally accepted mechanism for the generation of the high-valent iron-oxo intermediate Compound I in heme enzymes.[1,17] Protons also promote the conversion of the peroxo intermediate of MMO into the corresponding diiron(IV) oxidant **Q**.[3] In model systems, it has been demonstrated that acid facilitates O–O bond heterolysis for the conversion of acylperoxoiron(III) porphyrin complexes to oxoiron(IV) porphyrin cation radical species.[18] Proton-assisted O–O bond heterolysis of Fe^{III}–OOH intermediates to generate Fe^{V}=O oxidants is also proposed in the mechanisms of nonheme iron catalysts that use H_2O_2 as oxidant to carry out C–H hydroxylation, C=C epoxidation and *cis*-dihydroxylation, and aromatic ring hydroxylation.[19] The fact that many of the oxidations are highly stereoselective argues against the involvement of HO· species that would be produced from O–O bond homolysis.[19a] Indeed an EPR signal assigned to the putative Fe^{V} oxidant has been reported.[20] On the other hand, DFT calculations of Solomon and co-workers reveal a very significant barrier for O–O bond homolysis of high-spin Fe^{III}–OOH(R) species.[5] Taken together, the points presented above and our observed proton dependence for the conversion of **2** into **3** lead us to favor a heterolytic cleavage mechanism that would initially afford a formally Fe^{V}=O species. Unfortunately, our attempts to intercept the putative Fe^{V}=O species have not been successful. Owing to the neutral nature of TMC ligand, it is perhaps not surprising for the putative $[Fe^{V}(O)(TMC)]^{3+}$ species to have such a short lifetime; it could be rapidly reduced by one of several possible reductants present in the reaction mixture such as H_2O_2, NEt_3, or even the CH_3CN solvent to afford **3** that is experimentally observed (Scheme 1B). Indeed the only well characterized Fe^{V}=O complex to date is supported by a tetraanionic macrocyclic ligand that significantly extends the lifetime of the Fe^{V}=O unit.[21]

In summary, we report here the first example of a synthetic high-spin Fe^{III}–OOH complex that quantitatively converts to an oxoiron(IV) complex via O–O bond cleavage. This transformation is promoted by two factors: a) the strong Fe–O bond found for **2** as indicated by its high Raman frequency, which appears to prevent Fe–O bond scission even in the presence of 0.1 M $HClO_4$, and b) the key role of protons. Irrespective of the precise nature of the cleavage mechanism, the conversion of **2** to **3** demonstrates that O–O bond cleavage

can indeed occur readily at a high-spin iron(III) center, even at −40 °C. This example thus serves as a synthetic precedent for the proton-assisted conversion of high-spin Fe^{III}–OOH intermediates to high-valent iron-oxo oxidants in the proposed mechanisms of dioxygen-activating nonheme enzymes such as the *cis*-dihydroxylating Rieske dioxygenases[2] and bacterial multi-component monooxygenases like MMO_3 and toluene monooxygenase.[22]

Supplementary Material

Refer to Web version on PubMed Central for supplementary material.

Acknowledgments

We are grateful for support provided by NIH grants GM-33162 and GM-38767 (L.Q.) and EB-001475 (E.M.), NIH postdoctoral fellowships ES017390 (M.A.C.) and GM093479 (K.V.H.), and a University of Minnesota Doctoral Dissertation Fellowship (F.L.). We are indebted to Dr. Erik R. Farquhar for helpful guidance and discussion on the XAS analysis of **1** and **2** and to Dr. Jason England for insightful discussions.

References

1. (a) Denisov IG, Makris TM, Sligar SG, Schlichting I. Chem Rev. 2005; 105:2253–2278. [PubMed: 15941214] (b) Sligar SG, Makris TM, Denisov IG. Biochem Biophys Res Commun. 2005; 338:346–354. [PubMed: 16139790] (c) Watanabe Y, Nakajima H, Ueno T. Acc Chem Res. 2007; 40:554–562. [PubMed: 17567089]
2. (a) Kovaleva EG, Neibergall MB, Chakrabarty S, Lipscomb JD. Acc Chem Res. 2007; 40:475–483. [PubMed: 17567087] (b) Neibergall MB, Stubna A, Mekmouche Y, Münck E, Lipscomb JD. Biochemistry. 2007; 46:8004–8016. [PubMed: 17567152]
3. (a) Lee SK, Lipscomb JD. Biochemistry. 1999; 38:4423–4432. [PubMed: 10194363] (b) Tinberg CE, Lippard SJ. Biochemistry. 2009; 48:2145–12158.
4. (a) Kurtz DM Jr. J Inorg Biochem. 2006; 100:679–693. [PubMed: 16504301] (b) Kovacs JA, Brines LM. Acc Chem Res. 2007; 40:501–509. [PubMed: 17536780]
5. (a) Solomon EI, Decker A, Lehnert N. Proc Nat Acad Sci USA. 2003; 100:3589–3594. [PubMed: 12598659] (b) Lehnert N, Ho RYN, Que L Jr, Solomon EI. J Am Chem Soc. 2001; 123:12802–12816. [PubMed: 11749538]
6. Low-spin Fe^{III}–OOH complexes: (a) Simaan AJ, Döpner S, Banse F, Bourcier S, Bouchoux G, Boussac A, Hildebrandt P, Girerd JJ. Eur J Inorg Chem. 2000:1627–1633.(b) Roelfes G, Vrajmasu V, Chen K, Ho RYN, Rohde JU, Zondervan C, la Crois RM, Schudde EP, Lutz M, Spek AL, Hage R, Feringa BL, Münck E, Que L Jr. Inorg Chem. 2003; 42:2639–2653. [PubMed: 12691572] (c) Mairata i Payeras A, Ho RYN, Fujita M, Que L Jr. Chem–Eur J. 2004; 10:4944–4953.(d) Shearer J, Scarrow RC, Kovacs JA. J Am Chem Soc. 2002; 124:11709–11717. [PubMed: 12296737]
7. High-spin Fe^{III}–OOH complexes: (a) Wada A, Ogo S, Nagatomo S, Kitagawa T, Watanabe Y, Jitsukawa K, Masuda H. Inorg Chem. 2002; 41:616–618. [PubMed: 11849054] (b) Kitagawa T, Dey A, Lugo-Mas P, Benedict JB, Kaminsky W, Solomon E, Kovacs JA. J Am Chem Soc. 2006; 128:14448–14449. [PubMed: 17090014]
8. (a) Kim SO, Sastri CV, Seo MS, Kim J, Nam W. J Am Chem Soc. 2005; 127:4178–4179. [PubMed: 15783193] (b) Thibon A, England J, Martinho M, Young VG, Frisch JR, Guillot R, Girerd J-J, Münck E, Que L Jr, Banse F. Angew Chem, Int Ed. 2008; 47:7064–7067.(c) Hong S, Lee YM, Shin W, Fukuzumi S, Nam W. J Am Chem Soc. 2009; 131:13910–13911. [PubMed: 19746912] (d) Lee YM, Hong S, Morimoto Y, Shin W, Fukuzumi S, Nam W. J Am Chem Soc. 2010; 132:10668–10670. [PubMed: 20681694]
9. Annaraj J, Suh Y, Seo MS, Kim SO, Nam W. Chem Commun. 2005:4529–4531.
10. Schmidt M, Scherk C, Iakovleva O, Nolting HF, Meier B, Parak F. Inorg Chim Acta. 1998; 275:65–72.
11. The high-spin state for **2** results from constraints imposed by the TMC macrocycle that prevent formation of shorter Fe–N bonds required for a low-spin iron(III) center.

12. (a) Brunold TC, Solomon EI. J Am Chem Soc. 1999; 121:8277–8287.(b) Shiemke AJ, Loehr TM, Sanders-Loehr J. J Am Chem Soc. 1984; 106:4951–4956.
13. Katona G, Carpentier P, Nivière V, Amara P, Adam V, Ohana J, Tsanov N, Bourgeois D. Science. 2007; 316:449–453. [PubMed: 17446401]
14. Rohde JU, In JH, Lim MH, Brennessel WW, Bukowski MR, Stubna A, Münck E, Nam W, Que L Jr. Science. 2003; 299:1037–1039. [PubMed: 12586936]
15. Li F, England J, Que LJ Jr. J Am Chem Soc. 2010; 132:2134–2135. [PubMed: 20121136]
16. On the other hand, neither changing the concentration of H_2O_2 nor switching solvent from CH_3CN to CD_3CN affected the k_{obs}(500) and k_{obs}(820) values.
17. (a) Aikens J, Sligar SG. J Am Chem Soc. 1994; 116:1143–1144.(b) Vidakovic M, Sligar SG, Li H, Poulos TL. Biochemistry. 1998; 37:9211–9219. [PubMed: 9649301] (c) Dunford HB, Hewson WD, Steiner H. Can J Chem. 1978; 56:2844–2852.
18. Groves JT, Watanabe Y. J Am Chem Soc. 1988; 110:8443–8452.
19. (a) Chen K, Costas M, Kim J, Tipton AK, Que L Jr. J Am Chem Soc. 2002; 124:3026–3035. [PubMed: 11902894] (b) Mas-Ballesté R, Que L Jr. J Am Chem Soc. 2007; 129:15964–15972. [PubMed: 18052063] (c) Chen MS, White MC. Science. 2007; 318:783–787. [PubMed: 17975062] (d) Makhlynets OV, Das P, Taktak S, Flook M, Mas-Ballesté R, Rybak-Akimova EV, Que L Jr. Chem–Eur J. 2009; 15:13171–13180.(e) Joon Y, Wilson SA, Jang YK, Seo MS, Nehru K, Hedman B, Hodgson KO, Bill E, Solomon EI, Nam W. Angew Chem Int Ed. 2009; 48:1257–1260.(f) Chen MS, White MC. Science. 2010; 327:566–571. [PubMed: 20110502] (g) Das P, Que L Jr. Inorg Chem. 2010; 49:9479–9485. [PubMed: 20866083] (h) Makhlynets OV, Rybak-Akimova EV. Chem–Eur J. 2010; 16:13995–14006.
20. Lyakin OY, Bryliakov KP, Britovsek GJP, Talsi EP. J Am Chem Soc. 2009; 131:10798–10799. [PubMed: 19722657]
21. Tiago de Oliveira F, Chanda A, Banerjee D, Shan X, Mondal S, Que L Jr, Bominaar EL, Münck E, Collins TJ. Science. 2007; 315:835–838. [PubMed: 17185561]
22. Song WJ, McCormick MS, Behan RK, Sazinsky MH, Jiang W, Lin J, Krebs C, Lippard SJ. J Am Chem Soc. 2010; 132:13582–13585. [PubMed: 20839885]

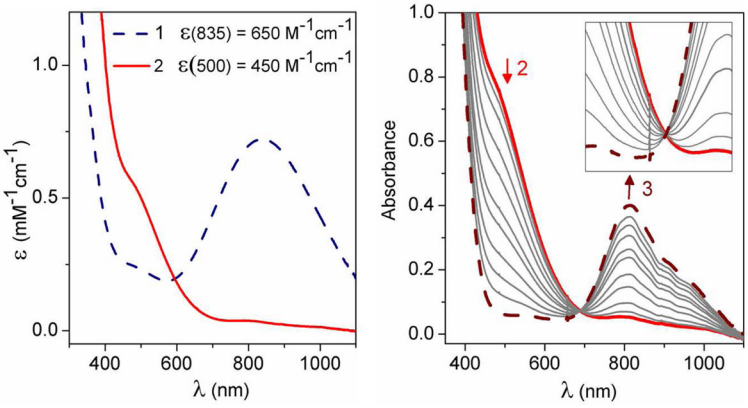

Figure 1.

Left: UV-visible absorption spectra of $[Fe^{III}(TMC)(O_2)]^+$ (**1**) (blue dashed line) and $[Fe^{III}(TMC)(OOH)]^{2+}$ (**2**) (red solid line) in CH_3CN. Right: UV-visible absorption spectra during the conversion of **2** (red solid line) to $[Fe^{IV}(O)(TMC)(CH_3CN)]^{2+}$ (**3**) (brown dashed line) via the addition of *ca.* 20 equiv. $HClO_4$ in CH_3CN at −40 °C. *b* = 1 cm. Inset: Close-up view to show the isosbestic point at ~695 nm.

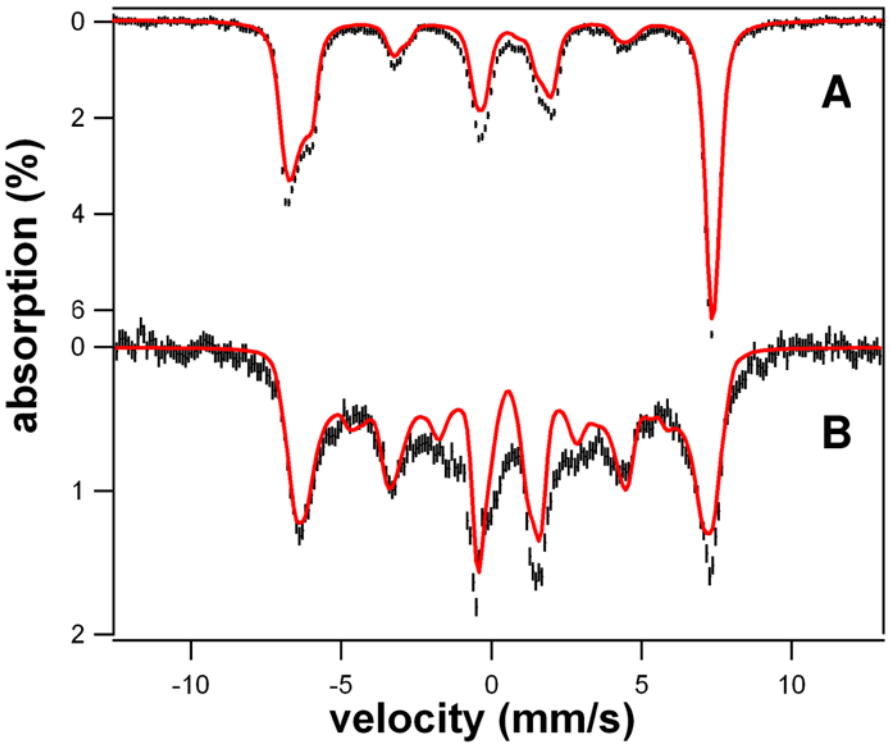

Figure 2.

4.2 K Mössbauer spectra of **1** and **2** in 3:1 PrCN/MeCN (v/v) recorded in parallel applied fields (black lines) and simulations (red lines); simulation parameters and comments are given in Table S1 and Supporting Information. (A) 8.0 T spectrum of **1**; same batch as used for EPR shown in Fig. 3A. (B) 1.2 T spectrum of **2**. The red line is a spectral simulation, assuming slow relaxation of the electronic system. 10% of **3** was removed from the data. Approximately 80% of the Fe in the sample belongs to **2.**

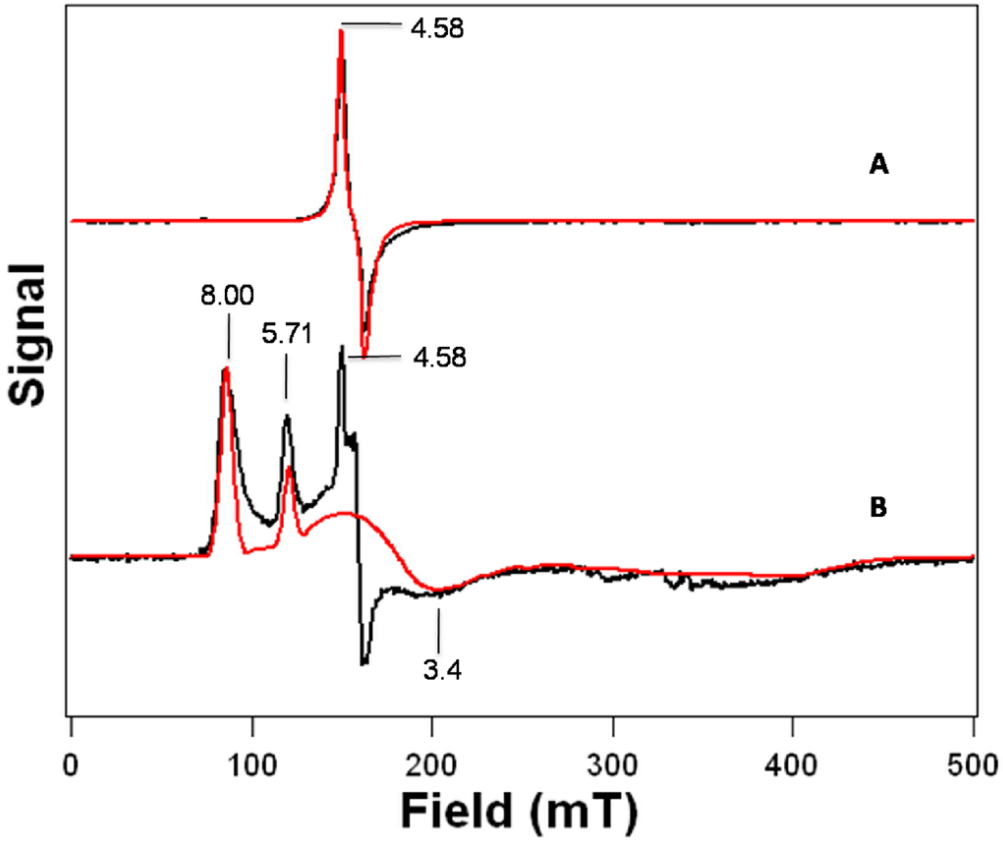

Figure 3.

X-band EPR spectra of **1** and **2** in 3:1 PrCN/MeCN (v/v) shown in black lines (A) Complex **1**. T = 15 K, microwave power, 0.02 mW, 1 mT modulation. The red line is a simulation using $D = -0.91\ cm^{-1}$, $E/D = 0.28$, fourth-order parameters $F = -0.108\ cm^{-1}$ and $a = -0.017\ cm^{-1}$ (see Supporting Information), $g = (2.04, 1.98, 2.03)$ and distributed E/D with $\sigma_{E/D} = 0.038$. (B) Complex **2**. T = 10 K, microwave power, 2.0 mW, 1 mT modulation. The red line is a simulation using $D = 2.5\ cm^{-1}$, $E/D = 0.097$, $g = (2.00, 2.00, 2.00)$, and $\sigma_{E/D} = 0.02$. The sharp features at $g_{eff} = 4.58$ and 4.36 represent remaining **1**, corresponding to (only) 1% of total Fe.

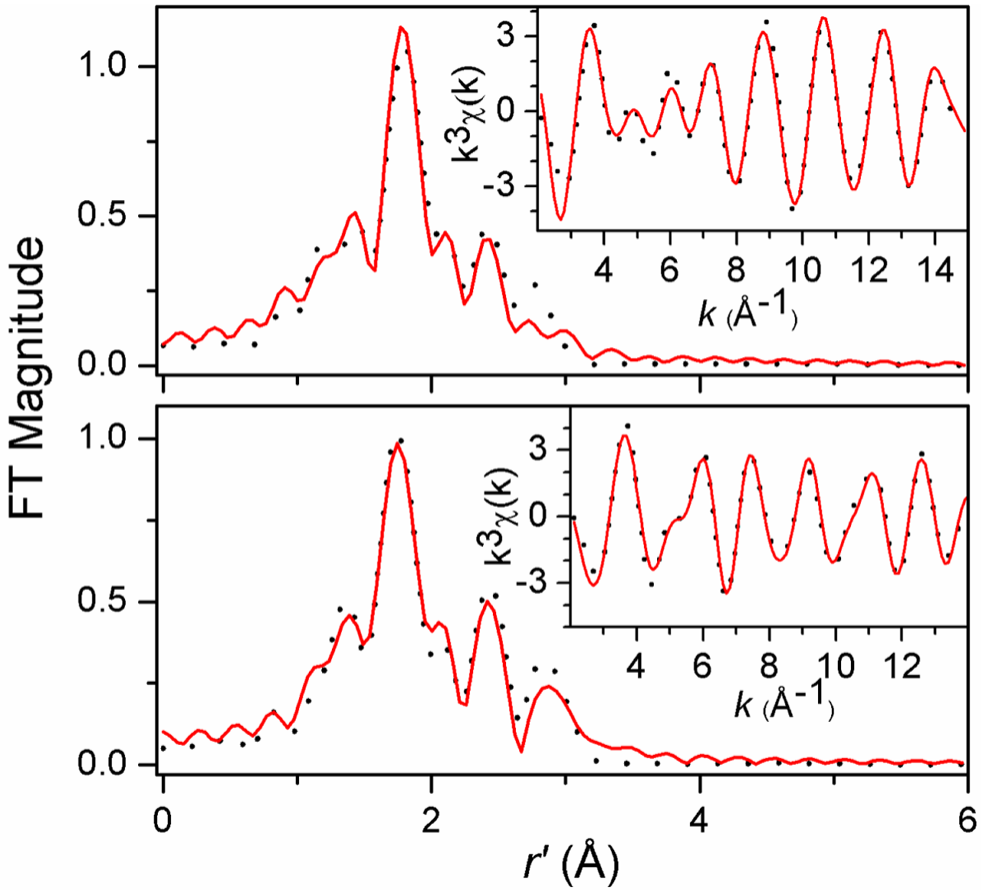

Figure 4.

Top: Fourier transform of Fe K-edge EXAFS of **1** (dotted line) over a *k*-range of 2–15 $Å^{-1}$ and a back-transformation range of 0.3–3.0 $Å^{-1}$. Inset: Fourier-filtered $k^3\chi(k)$ EXAFS data (dotted line). Solid lines represent fit 9 in Table S2. Bottom: Fourier transform of Fe K-edge EXAFS of **2** (dotted line) over a *k*-range of 2–14 $Å^{-1}$ and a back-transformation range of 0.3–3.2 $Å^{-1}$. Inset: Fourier-filtered $k^3\chi(k)$ EXAFS data (dotted line). Solid lines represent fit 9 in Table S3.

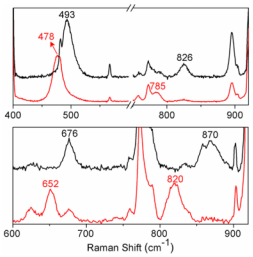

Figure 5.

Top: resonance Raman spectra of **1** prepared with H_2O_2 (black line) or H_2 $^{18}O_2$ (red line) and obtained with λ_{exc} = 647.1 nm. Bottom: resonance Raman spectra of **2** prepared with H_2O_2 (black line) or H2 $^{18}O_2$ (red line) and obtained with λ_{exc} = 514.5 nm.

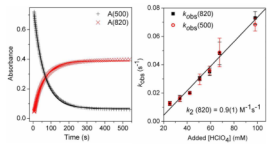

Figure 6.

Left: Plots of absorbance at 500 nm and 820 nm vs. time for the conversion of **2** to **3**. Solid lines represent fits of reaction progress (absorbance at 500 nm and 820 nm) against time to a typical first-order rate equation. Experimental conditions: 1.5 mM **2**, 34 mM $HClO_4$, −40 °C, in CH_3CN. Right: Plot of k_{obs}(820) and k_{obs}(500) vs. added [$HClO_4$] for the conversion of **2** to **3**. Experimental conditions: 1.5 mM **2**, −40 °C, in CH_3CN. The black line is a linear fit for k_{obs}(820). See Supporting Information for additional experimental details.

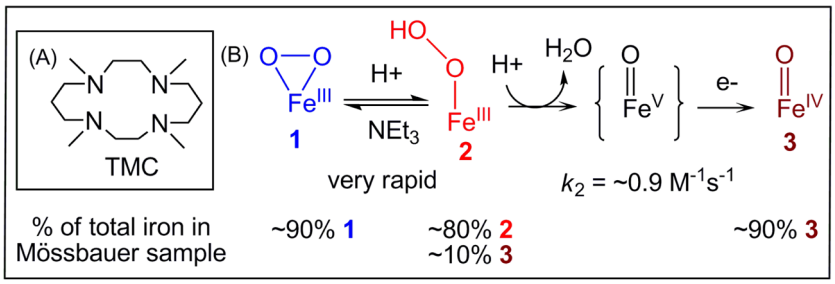

Scheme 1.

(A) TMC ligand used in this study. (B) Conversion of **1** to **2** and then to **3** via a putative short-lived Fe^{V}=O intermediate.

Table 1

Vibrational frequencies of high-spin Fe^{III}–OOH species.

Complexes[a]	ν(Fe–O), cm^{-1} ($\Delta^{18}O$) [$\Delta^{2}H$]	ν(O–O), cm^{-1} ($\Delta^{18}O$) [$\Delta^{2}H$]	ref
2	676 (−24) [−1]	870 (−50) [−1]	*b*
$[Fe(H_2bppa)(OOH)]^{2+}$	621 (−22)	830 (−17) [−4]	7a
E114A SOR	567 (−4)	838 (−23)	13
oxyhemerythrin	503 (−24) [−3]	844 (−48) [+4]	12
$[Fe(cyclam\text{-}PrS)(OOH)]^{+}$	419 (−19)	891 (−35) [*c*]	7b

[a] H_2bppa = bis(6-pivalamido-2-pyridyl-methyl)(2-pyridylmethyl)amine; SOR = superoxide reductase; cyclam-PrS = 1-(3′-mercaptopropyl)-1,4,8,11-tetraazacyclotetradecane anion.

[b] This work;

[c] Fermi doublet observed to collapse in deuterated solvent but no isotopic shift reported.